Study and Development of the Computer Model of Johnson-Cook Damage Criterion for Friction Spot Welding

Robson Cristiano Brzostek, rbrzostek@demet.ufrgs.br
Universidade Federal do Rio Grande do Sul
GKSS Research Centre/Institute of Materials Research-Materials Mechanics SolidState Joining Processes, Geesthacht, Germany.
José Antônio Esmerio Mazzaferro, mazza@ufrgs.br
Universidade Federal do Rio Grande do Sul/PROMEC-DEMEC, Porto Alegre, Rio Grande do Sul, Brazil.

Jorge Fernandes dos Santos, jorge.dos.santos@gkss.de
GKSS Research Centre/Institute of Materials Research-Materials Mechanics SolidState Joining Processes, Geesthacht, Germany.

Telmo Roberto Strohaecker, telmo@demet.ufrgs.br
Universidade Federal do Rio Grande do Sul/PPGEM-DEMET, Porto Alegre, Rio Grande do Sul, Brazil.

Abstract. *The Friction Spot Welding (FSpW) is a spot-like solid-state joining process that allows to joint two or more metal sheets in overlap configuration, suitable for welding lightweight materials. The main aim of this work is to study and develop a Johnson-Cook damage criterion model to represent the crack initiation, coalescence and the final fracture, allowing a better understanding of the fracture phenomenon in FSpW. The Johnson-Cook (JC) damage criterion considers no kinematic hardening and expresses rather the equivalent stress as a function of plastic strain, strain rate and the temperature. The base materials used were AA 2024-T351 and alclad AA 2024-T351 aluminum alloys. The parameters of JC were calculated and tested numerically. The numerical model results obtained shown good agreement with the experimental tests.*

Keywords*: Friction Spot Welding, Johnson-Cook damage criterion, fracture*

1. INTRODUCTION

Nowadays many efforts are being applied in the development of lightweight materials, especially in the automotive and aircraft industries. The developments point to a better use of the fuel, saving money and complying with environmental laws that restrict the emission of gases. Consequently, these increase on the use of lightweight materials result in many mechanicals components produced by different processes, which need to be joined. So far, resistance and laser spot welding as well as riveting and clinching processes have been the most commonly used joining techniques for such purposes (Pan et al., 2005).

Two relatively new solid-state spot welding processes called Friction Stir Spot Welding (FSSW) and Friction Spot Welding (FSpW) are still under development. Both friction based spot processes have proven to be able to produce high quality spot welds and to have high potential applicability in the industry. Some important characteristics of these processes are to be environmentally friend (no fumes, spatters or sparks are generated), allow solid-state welding, ease of automation, possibility of joining dissimilar materials, joining of materials difficult to weld by conventional fusion welding process, production of low distortion joints with excellent mechanical properties. (Silva et al., 2007).

The FSpW process was developed and patented by GKSS Forschungszentrum. The potential applicability of FSpW for structural and non-structural components is extremely high and since no bulk melting occurs it becomes an important alternative to fusion welding techniques. The technological advantages of this process are no need for additional material, minimal or no waste products, no post processing is necessary due to good surface quality, fast processing times and ease automation.

From the physical point of view, ductile damage is essentially atomic decohesion following dislocations pilling in metals, or growth and coalescence of cavities induced by large deformations. From the mechanical point of view, the fracture is the growth of a spherical or elliptical hole in a plasticity medium subjected to large strains, and the problem can be solved analytically or numerically. From the Continuum Damage Mechanism point of view, this is a reduction of the resisting area in any plane of a Representative Volume Element that is governed by the elastic energy and the Accumulate Plastic Strain. From this point of view various fracture models have been proposed to quantify the damage associated with material deformation and are used to predict fracture initiation.

2. FRICTION SPOT WELDING

2.1. Friction Spot Welding Characteristics

The FSpW process is performed by pressing a three-part rotating tool, composed by pin, sleeve (or shoulder) and clamping ring, into the workpieces producing frictional heat. The FSpW welding process consist of four steps, as can be seen in the Fig 1, in the first stage the sheets are fixed by pressing the clamping ring against the upper sheet surface,

while the pin and the sleeve start to rotate. On the second stage one of the spindles plunges into the sheets while the other one moves upwards creating space (reservoir) for a accommodating the plasticized material being squeezed by the plunging spindle. On the third step the process is reversed and both pin and sleeve retract back to the surface of the upper sheet. Doing so, the spindle moving downwards brings the plasticized material initially displaced back to its original position, refilling the hole left by the plunging spindle. On the fourth step the clamping load is released and the entire welding tool is withdrawn. The advantage of the shoulder plunge over the pin plunge variant is a bigger joint area which leads to a stronger joint. On the other hand the pin plunge is easier to perform since demands less power form the welding machine (Rosendo et al., 2007, Silva et al., 2007a, Silva et al., 2007b).

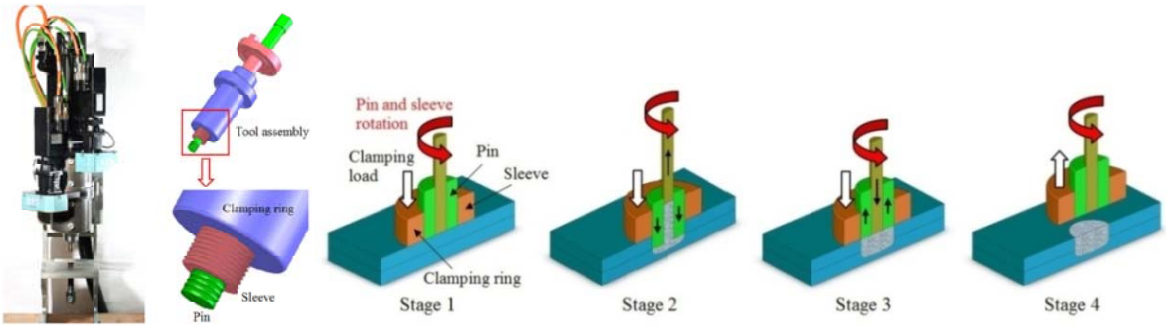

Figure 1 – The FSpW Equipment - Stages of the friction spot welding sleeve plunge variant.

2.2. Material Properties

The materials used were the aluminium alloy AA 2024-T351 with and without a corrosion protection clad layer. The AA 2024 has copper and magnesium as the alloying elements. It is used in applications requiring high strength to weight ratio, as well as good fatigue resistance, but it is not readily weldable by conventional arc welding processes. The T351 temper heat-treatment increases the mechanical properties. In aluminium with high purity the corrosion resistance due to thin surface layer of aluminium oxide that forms when the metal is exposed to the air effectively prevents further oxidation. However, in aluminium alloys where copper is the major alloying element, for electrochemical effects the corrosion can be strong because of two main factors: greater change in electrode potential with variations in amount of copper in solid solution and, under some conditions, presence of no conformities in solid-solutions concentrations. The general resistance to corrosion reduction with increasing copper content is primarily due to galvanic cells created by formation of minute copper particles or films deposited on the alloy surface as a result of corrosion. To increase the corrosion resistance they are often clad with high-purity aluminium, a low magnesium-silicon alloy. The cladding usually from 2.5 to 5% of the total thickness on each side, not only protects the composite due to its own inherently excellent corrosion resistance, but also exerts a galvanic effect which protects more the material (Weast, 1981, Ross, 1991, Nayer, 1997).

2.3. Experimental Results

In this work several AA 2024-T351 FSpW overlap joints were produced using different process parameters. The microscopic investigations along the cross section of all weld joints indicated distinct weld zones: the Stir Zone (SZ) the Thermo-Mechanical Affect Zone (TMAZ), the Heat Affected Zone (HAZ), and the Base Metal (BM), as shown in the Fig. 2.

Figure 2 - Cross section of FSpW joint to Unclad AA 2024-T351, showing the limits of the weld zones.

The SZ is a refined and rather equiaxied grains region, this typical microstructure appearance indicates that dynamic recrystallization takes place in this weld zone. The high deformation level and high peak temperature during welding in the SZ characterize such final grain structure. The TMAZ microstructure is characterized by grains distorted in comparison to the base material due to the high strain rate associated to a lower peak temperature in comparison to the weld centre. A higher magnification of this weld zone revealed elongated grains bended upwards along the vicinity of the SZ.

The microhardness profile at the weld specimens cross section reveals changes in mechanical properties, as can be seen in the Fig. 3. The base material presents an average of $135HV_{0.5}$ which decreases in the HAZ to a minimum of $120HV_{0.5}$ in the interface between the TMAZ and HAZ. The hardness loss at the outer limits of the HAZ is associated mainly to recovery of the base material as rolled microstructure since the temperature at this region is not so elevated during the welding. The more close to the center of the weld, the higher is the peak temperature reached and the strengthening precipitates can be subject to coarsening and even solubilization. Coarsening is expected to be predominant in the TMAZ due to the thermocycle in this wed zone. (Rosendo et al., 2008, Rosendo et al., 2007, Silva et al., 2007a, Silva et al., 2007b, Schilling, 2000, Ramos, 2008).

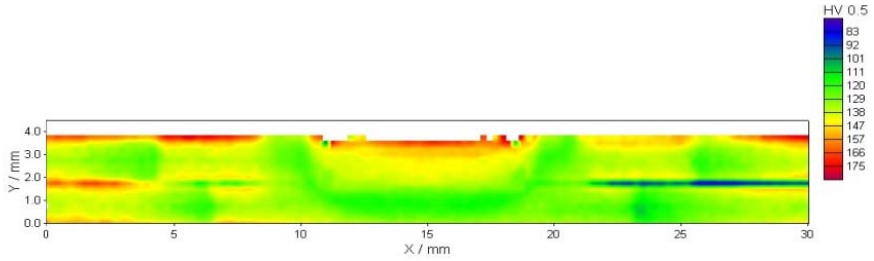

Figure 3 - Microhardness of Unclad AA 2024-T351 FSpW welding.

For the aluminium alloy with corrosion protection, the clad influence is evident, as can be seen in the macrograph shown in Fig. 4. The zones present in the joint were the same observed in the weld of the alloy without clad layer.

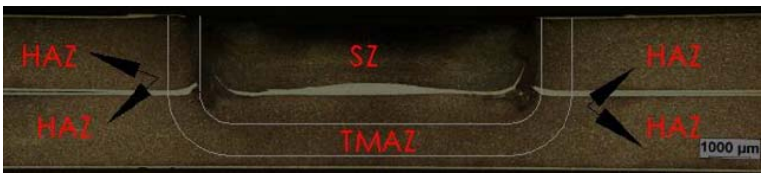

Figure 4 - Cross section of FSpW joint, to Alclclad AA 2024-T351, is showing the limits of the weld zones.

The microhardness of the joint evidences the clad presence by the occurrence of a zone with extremely low hardness in the middle the joint (interface between the two plates), as can be seen in the Fig. 5. It is possible to see the same different weld zones – SZ, TMAZ, HAZ, and BM. In the BM the hardness is $145HV_{0.5}$, this value decreases in the HAZ and TMAZ, while in the SZ there is an increase on the hardness, reaching the maximum value.

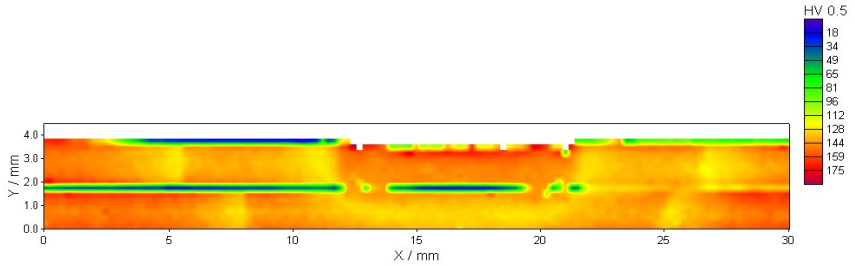

Figure 5 - Microhardness of Alclad AA 2024-T351 FSpW welding

For the numerical analysis two models were developed, one of them considering the clad influence and another without the clad layer. The sketch, shown in Fig. 6, was based in the macrograph images and microhardness profiles seen before, and has similar dimensions to both numerical models.

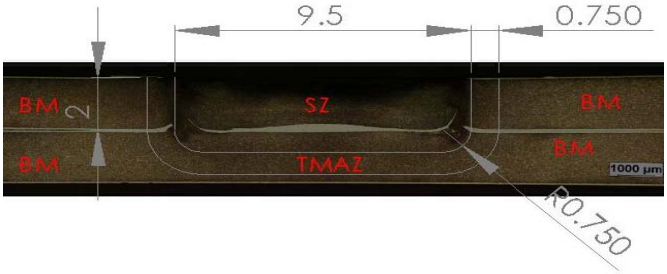

Figure 6 - The Sketch with dimensions used in the numerical model.

As described before, the joints of unclad aluminium plates have produced three different zones – BM, SZ, TMAZ, with different mechanical properties. The properties of base material were obtained by mechanical tests, while the properties of the other zones were defined based in the microhardness values observed in each zone. In the SZ an increase of 7.5% in resistance in relation to the BM was considered, while for TMAZ the resistance a decrease of 7.5%, when compared to BM, was adopted. In the model that considers the presence of the clad layer, the properties assigned to that region were the same of pure aluminium (1xxx series). Fig.7 presents the ultimate tensile strength values assigned to each zone for both material used.

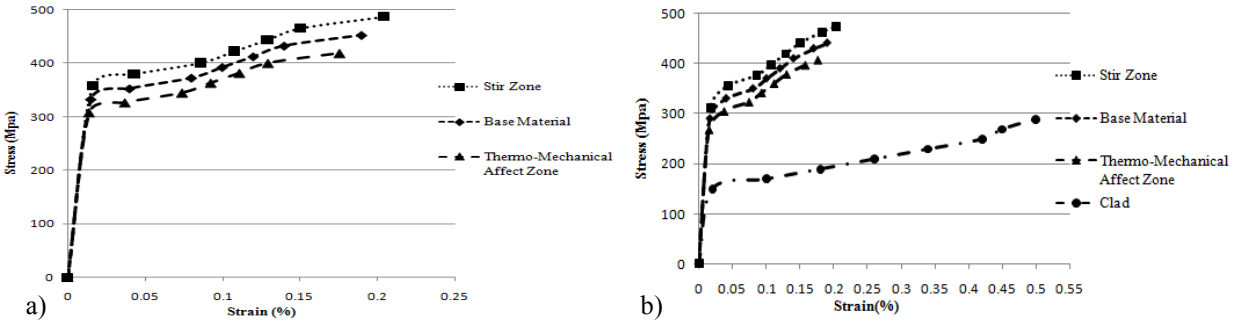

Figure 7 – Tensile Strength assigned to each zone of the joint; a) Unclad AA 2024-T351 b) Alclad AA 2024-T351.

3. DUCTILE DAMAGE

The ductile failure of a structure usually consists in three phases: (a) accumulation of damage; (b) initiation of fracture; (c) crack propagation. One way to think about fracture initiation is to consider it as result of the accumulation of ductile plastic damages. Microscopically, such damages are associated to void nucleation, growth and coalescence, shear ban movement and propagation of microcracks. Microscopically, degradation of the material exhibits decrease of the material stiffness, strength and reduction of the remaining ductility. These physical changes are often used as indicators to predict the onset of fracture, either based on the current value or in a cumulative fashion. In continuum damage mechanism, the material deterioration is described by an internal variable of the damage. In many applications, the damage can be considered isotropic but still gives good predictions and, therefore, is assumed as a scalar quantity herein. Damage should be distinguished and cannot be measured directly. To use cumulative damage as a criterion to predict the onset of fracture, the relationship between damage and some measurable parameters has to be established.

3.1. Ductile Criterion Model

The Ductile criterion is a phenomenological model for predicting the onset of damage. The model assumes that the equivalent plastic strain at the onset of damage, $\bar{\varepsilon}_D^{pl}$, is a function of stress triaxiality and strain rate: $\bar{\varepsilon}_D^{pl}\left(\eta, \dot{\bar{\varepsilon}}_D^{pl}\right)$, where $\eta = \frac{-p}{q}$, is the stress triaxiality, p is there pressure, q is the Mises equivalent stress, and $\dot{\bar{\varepsilon}}_D^{pl}$ is the equivalent plastic strain rate. The criterion for damage initiation is met when the state variable, ω_D, exceeds 1,

$$\omega_D = \int \frac{d\bar{\varepsilon}^{pl}}{\bar{\varepsilon}_D^{pl}\left(\eta, \dot{\bar{\varepsilon}}_D^{pl}\right)} = 1 \tag{1}$$

the state variable increases monotonically with plastic deformation. At each increment during the analyses the incremental increase ω_D is computed as, (Johnson and Cook, 1985, Lemaitre and Desmorat, 2005).

$$\Delta\omega_D = \frac{\Delta\bar{\varepsilon}^{\mathrm{pl}}}{\bar{\varepsilon}_D^{pl}\left(\eta, \dot{\bar{\varepsilon}}_D^{pl}\right)} \geq 0. \tag{2}$$

3.2. JOHNSON-COOK DAMAGE MODEL

Johnson and Cook have extended the damage model of ductile damage, presented in item 3.1, Eq. 1. They extended this strictly triaxial ratio dependent model so as to considerer high strain rates and high temperature effects on the strain to fracture of ductile metals, because plasticity and damage are impossible to distinguish during a tensile test.

The model is an accumulative-damage model that takes into account the loading story, which is represented by the strain to fracture, expressed as a function of the strain rate, temperature, and stress. This model is an instantaneous failure model, which means that no strength or stiffness remains after failure and failure is dynamic model is based on the value of the equivalent plastic strain at element integration points, failure assumed to occur when the damage parameter exceeds 1. The damage parameter, ω, is defined as

$$\omega = \sum \left(\frac{\Delta \bar{\varepsilon}^{pl}}{\bar{\varepsilon}_f^{pl}} \right) \tag{3}$$

where $\Delta \bar{\varepsilon}^{pl}$ is an increment of the equivalent plastic strain, $\bar{\varepsilon}_f^{pl}$ is the strain at failure, assumed to be dependent on a nondimensional plastic-strain rate

$$\bar{\varepsilon}_f^{pl} = \left[d_1 + d_2 e^{\left(d_3 \frac{p}{q} \right)} \right] \left[1 + d_4 \ln \left(\frac{\dot{\bar{\varepsilon}}^{pl}}{\dot{\varepsilon}_0} \right) \right] \left(1 + d_5 \hat{\theta} \right) \tag{4}$$

where $\frac{\dot{\bar{\varepsilon}}^{pl}}{\dot{\varepsilon}_0}$ is a nondimensional plastic-strain rate, $\frac{p}{q}$ pressure-stress ratio (where p is the pressure stress and q is the Mises stress) measures a triaxiality of the stress rate, $d_1 - d_5$ are failure measured constants, and $\dot{\varepsilon}_0$ is the reference strain rate and the nondimensional temperature $\hat{\theta}$,

$$\hat{\theta} \equiv \begin{cases} 0 & for\ \theta < \theta_{transition} \\ \frac{(\theta - \theta_{transition})}{(\theta_{melt} - \theta_{transition})} & for\ \theta_{transition} \leq \theta \leq \theta_{melt} \\ 1 & for\ \theta > \theta_{melt} \end{cases} \tag{5}$$

where θ, is the current temperature, θ_{melt} is the melting temperature, and $\theta_{transition}$ is the transition temperature (ABAQUS Documentation Version 6.8, 2009, Holmquist and Johnson, 1991, Traña, 2007).

3.2.1.1. Damage model's constants determination

To determine the damage model's constants, the strain to failure is established as a function of the triaxial state process, allowing to obtain the constants d_1, d_2, and d_3. After that, the parameter d_4 and temperature parameter, d_5, can be found. All parameters need characterization tests and numerical simulations.

3.2.1.1.1. Triaxial Stress State (d_1, d_2, and d_3)

At least, three tests must be made to build the exponential curve of the strain to fracture as a function of the triaxiality, $\frac{p}{q}$, and establish the corresponding parameters. In this study, the triaxiality characterization tests are made on isothermal condition.

Three different axissymetric tensile tests were performed to find the different stress triaxiality values to failure. To do so, specimens of different shapes, but with the same minimum cross section's diameter, were tested.

The state of stress that prevails inside the specimen at its failure is impossible to measure directly during the experiment. It is also hard to calculate it analytically from experimental measurement in uniaxial tensile test axissymmetric specimens. Even more, the triaxial state of stress changes during the loading process due to the notching.

After the triaxial states of stress are reached for each specimen, a best strain to failure versus triaxial ratio curve fit should be draw. The parameters that provide the best fit curves are then found by least square regression.

3.2.1.1.2. High strain rate stress state (d_4)

For the calculation of parameter d_4, only torsion tests at different shear strain rates are performed. Tests should cover the high strain rate regime that is experimented during the simulated phenomenon. Then few data points of shear strain to fracture at different strain rates are converted into equivalent strain to fracture with the Von Mises factors. With the equivalent strain at fracture data collected from quasi-static tests, a curve of the strain at fracture versus the strain rate can be drawn from quasi-static to high strain rates.

To obtain parameter d_4, a curve of a "reduced" strain failure $\left(\left(\varepsilon_f - (d_1 + d_2) \right) \right) / (d_1 + d_2)$ versus the strain rate should be drawn in natural semi-log graph. d_4 is then obtained as the slope of the curve. Note that this curve should be built from tests carried out at transition temperature.

3.2.1.1.3. High temperature environment (d_5)

The d_5 parameter is defined using the same technique used to define d_4, except that the shear strain to failure versus the shear strain rate curve must be generated at different temperatures. This experiment should be performed at temperatures that are close to that encountered in the problem to be modeled.

The temperature parameter d_5, is found by drawing a reduced strain to failure $\left(\left(\varepsilon_f - (d_1 + d_2) \right) \left(1 + d_4 \ln \left(\frac{\dot{\bar{\varepsilon}}^{pl}}{\dot{\varepsilon}_0} \right) \right) \right) \Big/ \left((d_1 + d_2)\, 1 + d_4 \ln \left(\frac{\dot{\bar{\varepsilon}}^{pl}}{\dot{\varepsilon}_0} \right) \right)$ versus temperature. All those should be

collected at high strain rates (ABAQUS Documentation, 2009, Holmquist and Johnson, 1991, Traña, 2007, Johnson and Cook, 1985).

3.2.1.2. Experimental results

To both studied materials, three different geometries were used to determine the strain to fracture at different state of stresses. The specimens that can be seen in the Fig. 8 exhibit a notch with different radius. Table 1 shows the most important parameters for the different specimens.

Table 1 - Dimensions of the specimens

	R(mm)	Φ(mm)	Φn(mm)
A	12	15	8
B	6	15	8
C	4	15	8

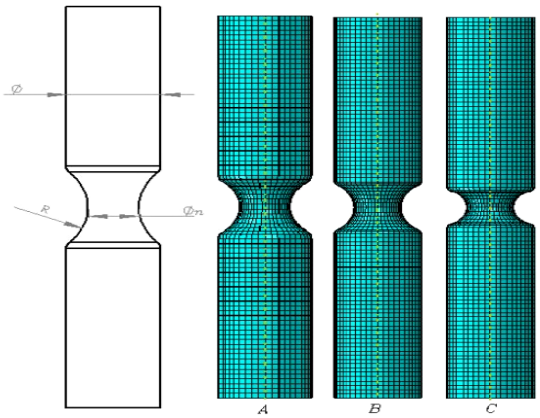

Figure 8 – Dimensions of the specimens tested

Simulations of tensile tests were performed to establish the pressure and the triaxial stress in the notch located in the middle of the specimens at instantaneous lengths. The results allow to plot the triaxial ratio as a function of the time, as can be seen in Fig. 9 to unclad AA 2024-T351. The stress values were obtained until they reach the maximum values before fracture in the uniaxial tensile test.

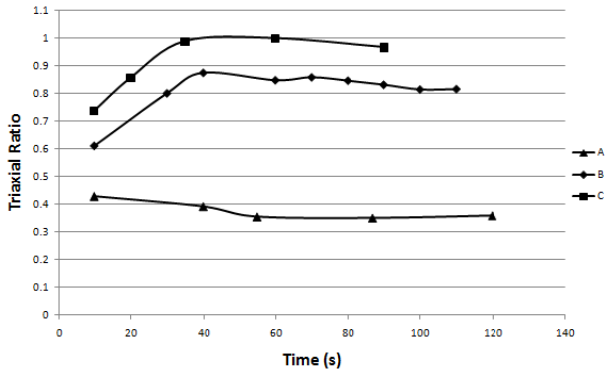

Figure 9 - Triaxial Ratio x Time for unclad AA 2024-T351.

The mean values obtained during the test until rupture are the triaxial ratio considered for the determination of the JC model constants. The failure strain is obtained by the best fit curve with the exponential adjustment method, as can be seen in the Fig. 10, thus the stress state constants d_1, d_2 e d_3 can be defined. With the values of these constants it is possible to determine the constant d_4 and, as this work does not consider the temperature influence, the constant d_5 is considered 0.

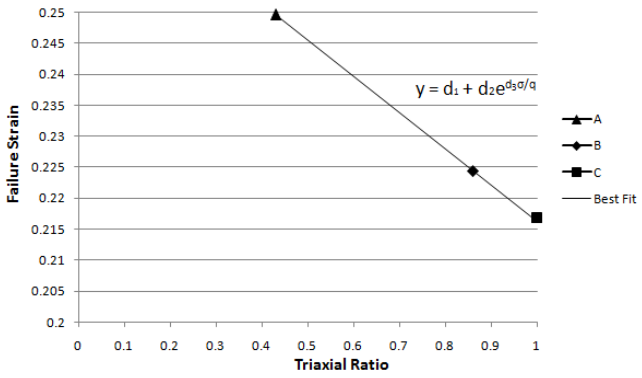

Figure 10 - Failure Strain x Triaxial Ratio for unclad AA 2024-T351.

The same method was used to determine the constants for Alclad AA 2024-T351. The relation between triaxial ratio and time is shown in Fig. 11-a, and the failure strain versus the triaxial ratio is presented in Fig. 11-b. Table 2 summarizes the JC parameters obtained to both materials.

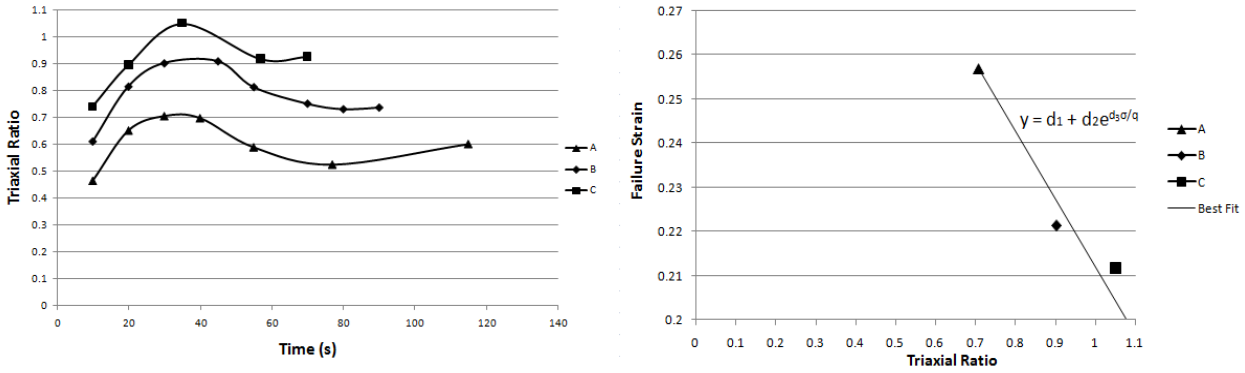

Figure 11 – a)Triaxial Ratio x Time to Alclad AA 2024-T35; b) Failure Strain x Triaxial Ratio to unclad AA 2024-T351

Table 2 - JC damage parameters.

	d_1	d_2	d_3	d_4	d_5	Reference Strain Rate
AA 2024-T351	0.15	0.18	-1.02	-0.011	0	1
AA Alclad 2024-T351	0.13	0.15	-1.112	-0.0678	0	1

To evaluate how the calculated constants represent the materials behaviour, the numerical model analysis of a tensile test was compared to the actual uniaxial tensile test. The results can be seen in the Fig.12-a, to AA 2024-T351 and in the Figure 12-b, to AA Alclad 2024-T351. A very good agreement between test and numerical results was observed, confirming that the parameters calculated represent well the phenomenon, therefore the constants can be used to analyse the fracture.

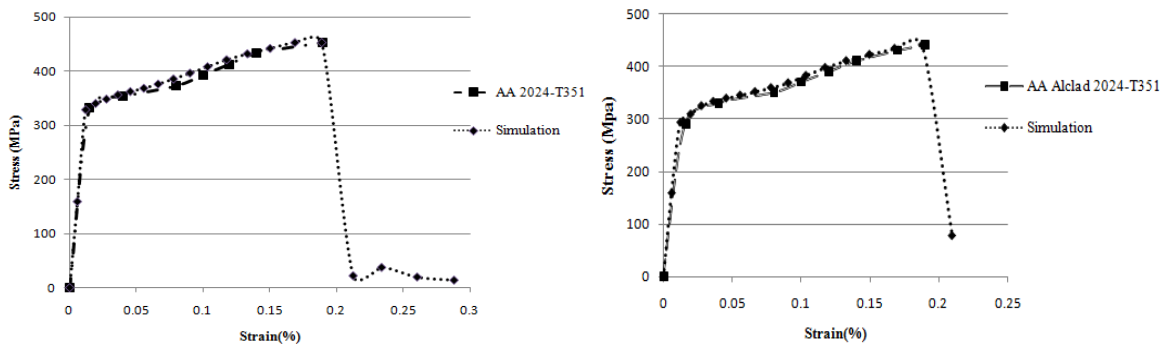

Figure 12 - Comparison of simulation with the actual test results a) to AA 2024-T351; b) AA Alclad 2024-T351.

4. FSPW JOINT MECHANICAL BEHAVIOUR

A numerical model was built to represent the lap-shear test specimen according to the standard DIN EN ISO 14272, as can be seen schematically in Fig. 13. In the test two plates welded by FSpW in overlap configuration are submitted to a uniaxial tensile load. The 3D solid is modeled as three different parts: an upper plate, a lower plate and a Stir Zone, assuming the properties shown in Fig. 7.

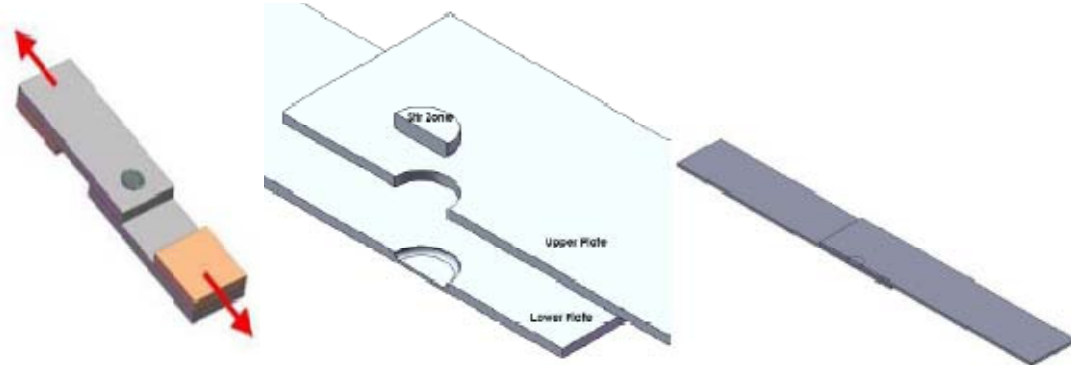

Figure 13 – Geometry of FSpW joint parts used in numerical model.

For the simulation of lap-shear test, just one half of the the actual specimen was modeled once there is symmetry of geometry and load across the vertical x-y plane as can be seen in Fig. 14. As shown in the figure, the extremity of the lower plate was pinned, what means that the displacement in the orthogonal x, y and z directions were set equal to zero. Also, the vertical movement of the external portion of both plates was not allowed, to reproduce the effect of shims that prevent out of load direction movements. To simulate the actual load condition experimented during the test a displacement of the external surface of upper plate in the x axis was specified. The surfaces of SZ in contact with the upper and lower plates were considered tied constrained, what means that there is no relative motion between them. This type of constrain fuses two regions even thought the meshes created on the surface of the regions may be dissimilar (Mazzaferro, 2008).

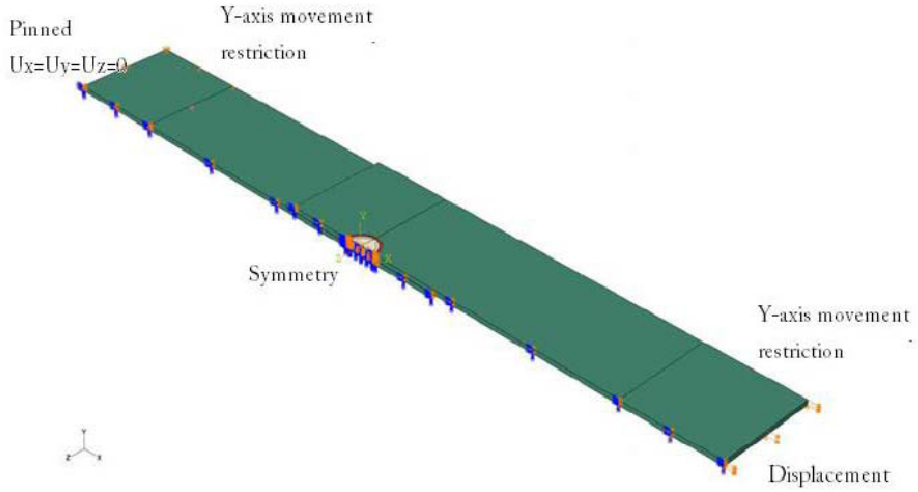

Figure 14 - Boundary conditions adopted for the shear test model.

4.1. Damage evolution

The damage evolution assumes that damage characterized by the progressive degradation of the material stiffness leading to material failure. For elastic-plastic material with isotropic hardening, the damage manifests itself in two forms: softening of the yield stress and degradation of the elasticity. The overall damage variable ω, Eq. 3, captures the combined effect of all damage mechanisms and is computed in terms of the individual damage variables, d_i. The value of the equivalent plastic strain failure, $\bar{\varepsilon}_f^{pl}$, Eq. 4, depends on the characteristic length of the element and cannot be used as a material parameter for the specification of the evolution law, instead, the damage evolution law is specified in terms of equivalent plastic displacement, $\bar{u}^{pl}$, or in terms of fracture energy dissipation, G_f, this energy is required to open a unit area of crack, and it is a material parameter. With this approach, the softening response after the damage

initiation is characterized by a stress-displacement response rather than a stress-strain response. The fracture energy is then given as,

$$G_f = \int_{\bar{\varepsilon}_0^{pl}}^{\bar{\varepsilon}_f^{pl}} L\,\sigma_y d\bar{\varepsilon}^{pl} = \int_0^{\bar{u}_f^{pl}} \sigma_y\, d\bar{u}^{pl} \tag{6}$$

where L, is characteristic length.

This expression introduces the definition of the equivalent plastic displacement, $\bar{u}^{pl}$, as the fracture work, conjugated of the yield stress after the onset of damage (work per unit area of the crack). Before damage initiation $\bar{u}^{pl} = 0$; after damage initiation $\bar{u}^{pl} = L\dot{\bar{\varepsilon}}^{pl}$. This definition of the characteristic length is used because the direction in which fracture occurs is not known in advance. The damage evolution based in effective plastic displacement, $\bar{u}^{pl}$, is defined as

$$\bar{u}^{pl} = L\dot{\bar{\varepsilon}}^{pl} \tag{7}$$

The evolution of damage variable with the relative plastic displacement can be specified in tabular, linear, or exponential form. Instantaneous failure will occur if the plastic at failure $\bar{u}_f^{pl}$, is specified 0.

In this work was assumed an exponential damage evolution of the damage variable given as

$$\omega = 1 - e^{\left(-\int_0^{\bar{u}^{pl}} \frac{\bar{\sigma}_y\, \bar{u}^{pl}}{G_f}\right)} \tag{8}$$

The exponential formulation of the model ensures that the energy dissipated during the evolution process is equal to G_f. In theory, the damage variable reaches value of 1 only asymptotically at infinite equivalent displacement. In practice, when the dissipated energy reaches a value of $0.99G_f$, ω will be set equals to on.

5. RESULTS AND DISCUSSION

For the AA 2024-T351 simulation and experimental tests, the fracture mode identified was plug pull-out, as can be seen in the Fig. 15, where the detail of element mesh separation is represented too.

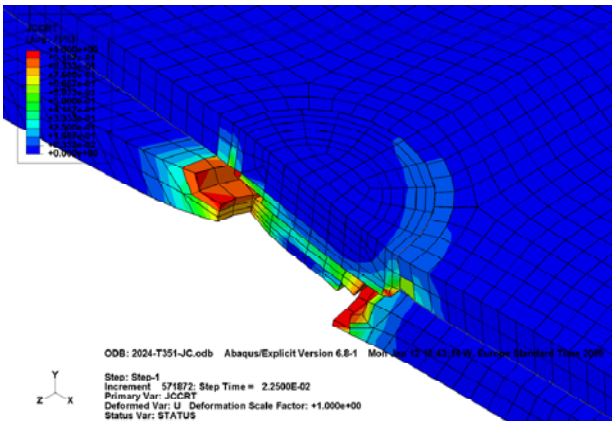

Figure 15 - The plug pull-out fracture.

In the Fig.16, the failure steps during simulation are represented, to allow a better visualization the upper plate was not shown. At the Fig. 16-a, the value of Johnson-Cook damage initiation criterion (JCCRT) is very near 1, on the region around SZ. After, at the Fig. 16-b, the elements that first reached the limit value of JCCRT were deleted. The crack begins when more elements were deleted as can be seen on the Fig. 16-c. Finally, the plug pull-out fracture occurs as shown in the Fig.16-d.

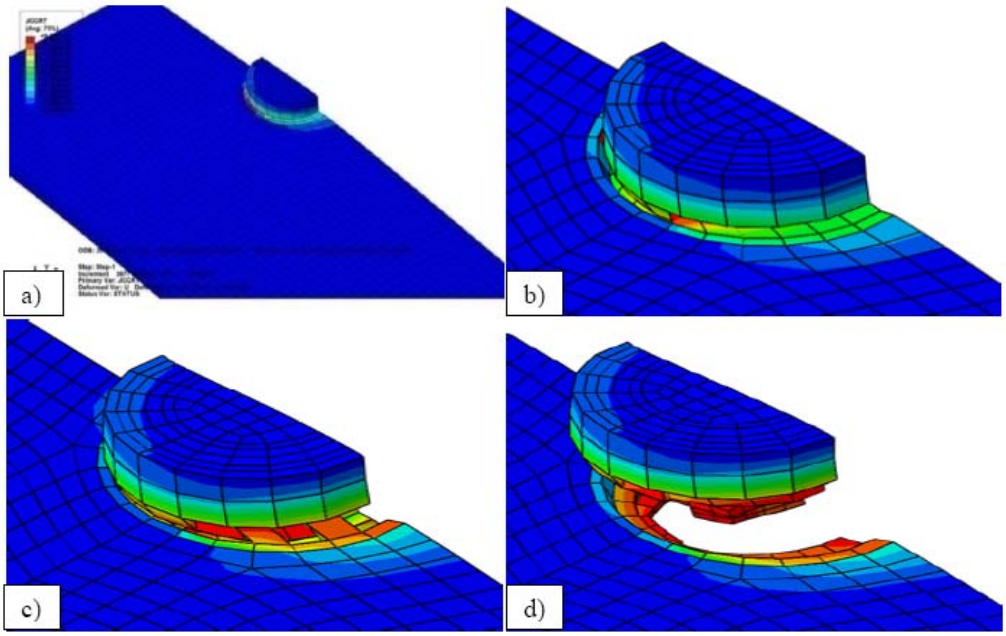

Figure 16 - Fracture steps - a) JCCRT is very close to 1; b) when the JCCRT is 1, some elements were deleted; c) some more elements were deleted; d) the fracture happens.

For the AA Alclad 2024-T351 simulation and experimental tests, the fracture mode identified was through weld accompanied by circumferential crack, as can be seen in the Fig.17.

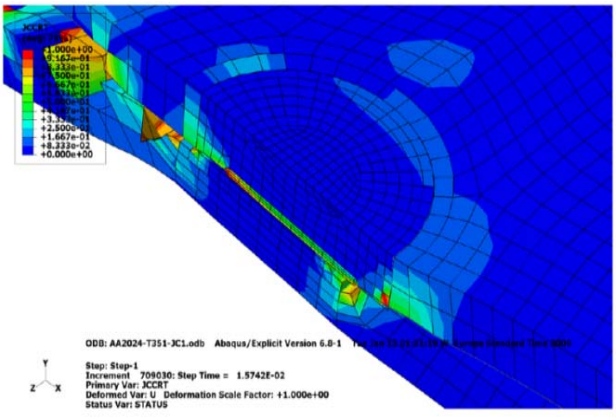

Figure 17 - Through weld accompanied by circumferential crack

The failure steps are shown in Fig. 17, to better visualization the upper plate was extract. In the Fig. 17-a, the value of Johnson-Cook damage initiation criterion (JCCRT) is very close to 1 around SZ. After, in the Fig. 17-b, the elements that first reached JCCRT limit value were deleted. The crack begins when more elements were deleted as can be seen on the Fig. 17-c. Finally, a through weld accompanied by circumferential crack fracture occurs, as shown in the Fig. 17-d.

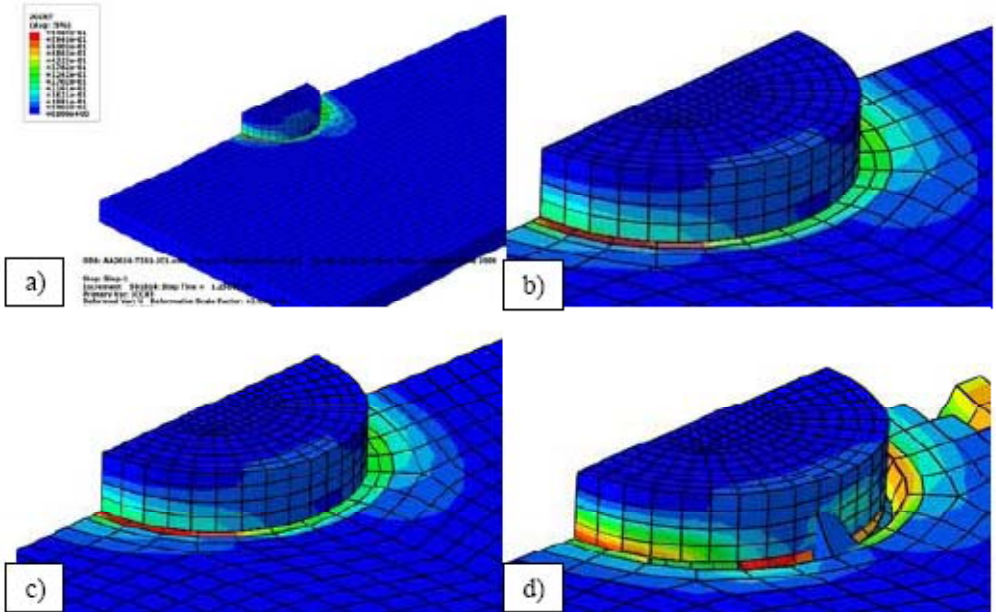

Figure 17 - Fracture steps - a) JCCRT is very near to 1; b) when the JCCRT is 1, some element were deleted; c) some more elements were deleted; d) the fracture happens.

6. CONCLUSIONS

The results of numerical model developed correspond to the fracture modes observed in lap-shear actual tensile tests. The simulations produced very similar fracture geometries when compared with experimental tests.

For unclad AA 2024 – T351 all simulations point to the initiation of the fracture occurring around the joining area, in the region of contact between the upper and lower plates where occurs the highest stress levels. The mode of fracture identified is plug pull-out.

To AA 2024 – T351 all simulations produced the through weld and circumferential crack mode of fracture.

To both models the fracture happens and the crack propagates around the SZ, where the higher stress levels occur.

7. REFERENCES

ABAQUS, 2009 - Documentation Version 6.8 – Licensee by GKSS- Forschungszentrum.

DIN EN ISO 14273 -Specimen Dimensions And Procedure For Shear Testing Resistance Spot, Seam And Embossed Projection Welds (Iso 4273:2000); German Version En Iso 14273:200.

Holmquist, T.J., Johnson, G.R. 1991- Determination Of Constants And Comparison Of Results For Various Constitutive Models – Journal De Physique Iv, Vol. 1, October.

Johnson, G. R., Cook, W. H., 1985 - Fracture Characteristics Of Three Metals Subjected To Various Strains, Strain Rates, Temperatures And Pressures, Engineering Fracture Mechanics, Vol. 21, No.1, Pp. 31–48.

Lemaitre,V. J.; Desmorat R.; 2005, Engineering Damage Mechanics: Ductile, Creep, Fatigue And Brittle Failures. Springer; 1 Edition, May 23,

Mazzaferro, J. A. E.; Rosendo, T. ; Mazzaferro, C. C. P. ; Ramos, F. D. ; Tier, M.A.D. ; Santos, Jorge Fernandez Dos ; Strohaecker, Telmo Roberto, 2008 - Study On Mechanical Behavior Of Friction Spot Welds. In: Iiw International Congress - Xxxiv Consolda , São Paulo. Anais Do Iiw International Congress - Xxxiv Consolda

Nayer, A., 1997 - The Metals Databook, , Mcgraw-Hill Companies, June 1

Pan, T., Zhu, W.; Schwarz, W., 2005, Spot Friction Welding For Aluminium Sheets. Proceedings Of The 2005 International Automotive Body Congress. Michigan, Usa, V. 2, Pp 95-99, September 20-21

Ramos, F., Rosendo, T.; Tier M. D. ; J. Mazzaferro; Mazzaferro, C. ; A. M. Da Silva ; Santos, J. F. ; Strohaecker, T. R., 2008, . The Influence Of The Tool Profile In Friction Stir Spot Welding For Aluminium Alloy Aa6181-T4. In: 8th International Conference On Trends In Welding Research, Georgia. Proceedings Of 8th International Conference On Trends In Welding Research.

Rosendo, T. ; Neussel, C. ; Tier M. D. ; Mazzaferro, C. ; Ramos, F. ; A. M. Da Silva ; Bayer, M. ; Santos, J. F. ; J. Mazzaferro ; Strohaecker, T. R. ; Isakovic, J., 2008 . Mikrostructure Und Eingenschaften Von Reibpunktgeschweissten Verbindugen Der Legierungen Aa7075-T6 Und Aa6181-T4. In: Fügetechniken Im Leichtbau, Dvm Tag 2008 Leichtbaustrategien, 2008, Berlim. Fügetechniken Im Leichtbau, Dvm Tag 2008 Leichtbaustrategien, 2008

Rosendo, A.A.M. Da Silva, M.A.D. Tier, F.D. Ramos, C.C.P. Mazzaferro, J.A.E. Mazzaferro, T.R. Strohaecker, J.F. Dos Santos., 2007 Preliminary Investigation On Friction Spot Welding Of Alclad 2024 T3 Aluminium Alloy. Xxxiii Consolda - Congresso Nacional De Soldagem. Caxias Do Sul, 27 – 30 De Agosto.]

Ross, R. B., 1991 - Metallic Materials Specification Handbook, Fourth Ed., Springer; 4th Edition (December 31)

Silva, A. A. M. ; Ramos, F. D. ; Souza, T. R. ; M.A.D.Tier ; Mazzaferro, C. C. P. ; Mazzaferro, J. ; Bergmann, L. ; Beyer, M. ; Isakovic, J ; Strohaecker, T. ; Dos Santos, J. F., 2007a, Microstructure And Properties Of Friction Spot Welds In A 2-Mm Thick Alclad Aa 202 T3. In: Fabtech & Aws Welding Show, 2007, Chicago. Proceedings Of Fabtech & Aws Welding Show, Chicago, Il Usa, November 11-14

Silva, A. A. M. ; Souza, T. R. ; Ramos, F. D. ; Mazzaferro, C. C. P. ; Mazzaferro, J. ; M.A.D.Tier ; Bergmann, L. ; Strohaecker, T. ; Dos Santos, J. F., 2007b Friction Based Spot Welding Processes Literature Review. In: Viii International Conference Of Isim Timisoara Innovative Technologies For Joining Advanced Materials, 2007, Timisoara. Viii International Conference Of Isim Timisoara Innovative Technologies For Joining Advanced Materials, Timisoara, Romania, 7-8 June, 2007

Schilling, C. 2000 - A Preliminary Investigation On The Static Properties Of Friction Stir Spot Welding. 2nd International Symposium Of Friction Stir Welding, Gothenburg, June 26-28,

Traña, E. 2007 – Plastic-Kinematic Vs Johnson-Cook Model In Fem Taylor Test Simulation, 11th International Research/Expert Conference, September

8. RESPONSIBILITY NOTICE

The authors are the only responsible for the printed material included in this paper.